Materials Research. 2022; 25:e20220202
DOI: https://doi.org/10.1590/1980-5373-MR-2022-0202

A Simple Method for Low-temperature Sintering of Titania

Anna Luísa W. R. Miguel*[a], *Roberto R. de Avillez*[a], *Marlin J. Pedrozo-Peñafiel*[b], *Ricardo Q. Aucélio*[b], *Sonia Letichevsky*[a]

[a]*Pontifícia Universidade Católica, Departamento de Engenharia Química e de Materiais, 22451-900, Rio de Janeiro, RJ, Brasil.*
[b]*Pontifícia Universidade Católica do Rio de Janeiro, Departamento de Química, 22451-900, Rio de Janeiro, RJ, Brasil.*

Received: April 19, 2022; Revised: August 30, 2022; Accepted: September 04, 2022

A low-temperature sintering process was used to produce pellets at different temperatures using TiO_2 anatase (Vetec) and P25 (Evonik) commercial powders. The initial powder was mixed with 75% acetic acid aqueous solution and pressed under 375 MPa. The temperature was applied after the pelletization in a conventional furnace for 4 hours. The best sintering temperature for anatase was 800°C, which is higher than typical cold sintering temperatures but below conventional ones. However, the optimal temperature was 450 °C for P25 due to its density and SEM results. The sintered pellets' maximum densities were 70% (anatase, 800°C) and 66% (P25, 450°C). It was not possible to measure the anatase pellets treated under 800°C because they disintegrated in water. This work studied the effects of the applied pressure, solvent concentration, particle size, and sintering temperature on the properties of sintered pellets, such as integrity, density, and presence of porous. It also evaluated the electrochemical activity measured by cyclic voltammetry (CV), which indicated that the sintered TiO_2 pellets are porous with a partial capacitive response.

Keywords: *titanium oxide, low-temperature sintering, anatase, P25, cyclic voltammetry.*

1. Introduction

Photocatalysts are employed in several industry segments and chemical processes. Generally, the smaller the particle size, the greater it is the surface area, improving reaction rate. It is often difficult to remove the photocatalyst from the reaction medium to be further reused due to its particles´ size. For instance, it is challenging to extract all of the dispersed photocatalyst powder after degrading the pollutant in water[1,2]. Although TiO_2 is usually considered an inert material, some authors have studied its toxicity and proved that its physicochemical properties could change with its size, so, in nanometers, TiO_2 is chemically more reactive. TiO_2 nanoparticles can influence some properties, making them desirable, such as the improvement of photocatalytic activity, or undesirable, such as toxicity, induction of oxidative stress, or even cellular dysfunction[3,4].

The transformation of the photocatalyst powder into a compact material in the form of ceramic supports is an alternative to facilitate its recovery[5,6]. Furthermore, it avoids the release of nano TiO_2 into the environment. However, the photocatalyst pellet must be porous to increase the surface area and favor water permeation. Besides, the pellet must be thin enough to allow the light to reach the inner grains. Therefore, the densification of the pellet must not be complete.

The most common ceramics densification process is sintering, which usually requires very high temperatures[7,8]. Conventional sintering is generally performed at temperatures over 1000°C, for many hours or even days. The sintering temperature is 50-75% of the of the material melting temperature and densifies the initial powder material with the assistance of thermal energy[8,9]. The high temperature favors the grain growth reducing the material's surface area per unit volume and may also cause phase transformations.

When a pellet is produced by mixing a powder and sintering above the solidus line, sintering proceeds in the presence of a liquid phase and it is the liquid-phase sintering (LPS). Solid-state sintering (SSS) occurs without the liquid phase at the sintering temperature. The pore-filling mechanism is justified for most LPS processes where grain shape can be considered to maintain an equilibrium shape[10].

Recently, a low-temperature sintering process was proposed[10]. The cold sintering process (CSP) is a new technique developed with pressure-assisted (100 -500 MPa) and low temperatures (no higher than 600 °C)[8,11]. This process uses aqueous or acidic solutions as solvents to promote the densification of the material by the dissolution-precipitation process[11]. CSP reviews were recently published[12,13]. Grasso et al.[14] reviewed all proposed low-temperature sintering processes that they called Ultra Low Energy Sintering (ULES). They stated that ULES is a process that uses "high pressure (hundreds of MPa) in the presence of a transient liquid phase" to accelerate plasticity, grain boundary/surface diffusion, and mass transport. They pointed out that the evaporation of the liquid phase is the novelty of the CSP compared to previous related processes. Surface free energy reduction is the main driving force for

*e-mail: letichevsky@puc-rio.br

sintering[15]. If the initial liquid phase evaporates, one may consider using it only during the green body preparation and make the sintering in a typical furnace. If the liquid phase reacts with the powder and solubilizes a small amount of compound, it may favor the compaction during the green body preparation. This small change is expected to reduce the sintering temperature while using conventional furnaces.

Titanium oxide (TiO_2) is a semiconductor oxide with multiple applications, especially important in pigment, food, and cosmetics[16]. TiO_2 is also used to decontaminate water and air through catalytic processes[17]. Anatase and rutile are the most common phases of TiO_2[8], but rutile is the thermodynamically stable phase at room temperature.

Catalytic and photocatalytic reactions associated with TiO_2 usually involve electron transfer and, therefore, redox chemical reactions that can be studied by cyclic voltammetry, a simple electrochemical technique commonly used to evaluate mechanisms of redox reactions and to characterize reactants and catalysts as the TiO_2 pellets[18].

This study describes the production of anatase and P25 ceramic pellets from commercial powders using a ULES, low-temperature sintering process, a variant of the cold sintering process with the addition of acetic acid solution as the transient liquid phase and the pressure applied before the sintering temperature. Acetic acid is used as the transient solvent required by low-temperature sintering processes. This solvent is responsible for the partial dissolution of the surface of the starting powder, creating a saturated solution around each particulate. The powders are pressed uniaxially, allowing the saturated solution to flow around the powders, creating a highly compacted green body even at room temperature. The green body is taken off the mold and heated in a conventional oven, which causes the evaporation of the acetic acid aqueous solution and the precipitation of particles that help to fill in the voids between the grain boundaries, favoring a denser ceramic[17]. Different characterization techniques were used to understand the sintering process and the electrochemical activity of sintered TiO_2 pellets.

2. Experimental

2.1. Sintering of anatase pellets

Each pellet was produced with 0.30 g of TiO_2 anatase powder (VETEC ®) sieved below 53 μm and mixed with an aqueous acetic acid solution (Merck ® - Germany) in different concentrations and volumes. Samples An1 and An2 (Table 1) were prepared by mixing the TiO_2 powder with 0.10 mL of aqueous acetic solution at 25% and 50% (v/v), respectively. An was prepared with 0.10 mL of ultrapure water (resistivity < 8MΩ cm) obtained from a water purifier Milli-Q Gradient System A10 (Millipore, USA). Samples An200, An400, and An800 were prepared using 0.15 mL of 75% acetic acid solution[19]. The number after An refers to the temperature applied after the pellet formation. The solution volumes added to the material were optimized due to the changes in the water proportion. The solution must not soak the material to avoid spilling out of the mold but keeping it moist[8].

The pressure and time used for the pelletization were obtained experimentally after some optimization tests. The mixtures were placed in the mold and pressed at 624 MPa or 375 MPa[8] for 15 minutes. After that, the pellets (Figure S1) were removed from the mold (Figure S2) and transferred to a conventional furnace at 200 ºC, 400 ºC, or 800 ºC for 4 hours. At least three pellets were prepared for each sintering temperature.

2.2. Sintering of P25 pellets

The P25 pellets production was similar to the anatase pellets. 0.30 g of P25 (supplied by Evonik®) was mixed with 0.10 mL of 75% aqueous acetic acid solution. Then the mixture was placed in the mold and pressed at 375 MPa for 20 minutes. The pressure was determined from the previous results obtained with the anatase pellets. Finally, the pellets were submitted to 200 ºC (P200), 400 ºC (P400), 450 ºC (P450), or 500 ºC (P500) for 4 hours in a conventional furnace. The maximum temperature was 500 ºC to prevent the anatase phase transformation into rutile[8]. At least three P25 pellets were produced for each sintering temperature.

2.3. Characterization

FTIR analysis was performed using the FT-IR Spectrometer Spectrum Tow, Perkin-Elmer, in the 4000 cm^{-1} to 400 cm^{-1} wavenumber range and a scan number of 50. FTIR analyses were performed for samples P450, P400, and An800, as well as raw anatase and P25 powders. In addition, new P25 samples were prepared: with water (PH_2O) and 75%

Table 1. Sintering parameters for anatase and P25 pellets.

Sample	Sintering temperature (°C)	Pressure (MPa)	Concentration of acetic acid aqueous solution (% v/v)	Volume (mL)	Mass (g)
An	400	624	0	0.10	0.25
An1	400	624	25	0.10	0.25
An2	400	624	50	0.10	0.25
An4	400	624	75	0.15	0.30
An5	400	624	100	0.15	0.30
An200	200	375	75	0.15	0.30
An400	400	375	75	0.15	0.30
An800	800	375	75	0.15	0.30
P200	200	375	75	0.10	0.30
P400	400	375	75	0.10	0.30
P450	450	375	75	0.10	0.30
P500	500	375	75	0.10	0.30

aqueous acetic acid solution (PHAc), both dried at room temperature. A third pellet (P250) was prepared with the same aqueous acetic acid solution used for PHAc, but instead of natural drying, P250 was submitted to 250°C for 1 hour in a typical furnace. Anatase pellets AnHAc and An250 were produced using TiO_2 anatase from Vetec using the same procedure for PHAc and P250, respectively.

TG/DSC analysis was performed for the anatase and P25 pressed samples in a Simultaneous Thermal Analyzer STA-600, Perkin-Elmer, using 10 mg of the sample with temperature range from 30 ºC to 600 ºC at a heating rate of 10 ºC min^{-1}, under a N_2 flow of 20 mL min^{-1}.

X-ray diffraction patterns were collected for the sintered pellets and the raw anatase and P25 powders using a Bruker D8 Discover diffractometer with CuKα radiation, Bragg-Brentano geometry, nickel filter, and a Lynxeye detector. The crystalline phases and their crystallite sizes were determined by the Fundamental Parameters Approach, FPA, Rietveld refinement method in Profex/BGMN program[20]. The FPA in Profex/BGMN is a ray-tracing program that calculates the instrumental peak profile based on the diffractometer geometry and allows the crystallite size estimation after deconvoluting the instrument profile contribution[21,22]. So, the Scherrer equation and its variations from kinematical theory for X-ray diffraction provide acceptable crystallite sizes up to 600 nm[23].

The pellets' density was determined by the Archimedes method[24]. Each measurement was performed at least five times to evaluate the error.

The morphology of the pellets' surface was characterized by a scanning electron microscope equipped with an Energy Dispersive X-Ray Spectroscopy (SEM/EDS - HITACHI, TM3000 – Tabletop Microscope and EDS SwiftED3000).

Cyclic voltammetry was used for the electrochemical characterization of the sintered material. CV was performed using a BAS voltammetric analyzer CW-50, applying a scan rate of 50 mV s^{-1}. The electrochemical cell (8 mL volume) was made of Teflon with openings to adapt the auxiliary electrode (Pt wire), the reference electrode (Ag/AgCl ($KCl_{(sat)}$)), and the working electrode (anatase or P25 pellets). The supporting electrolytes were 0.1 mol L^{-1} potassium hydroxide (KOH) solution[17], obtained from VETEC© for anatase pellets, and 0.5 mol L^{-1} sodium phosphate dibasic (Na_2HPO_4) solution[25], also obtained from VETEC©, for P25 pellets. The potential range of -1500 mV to +1500 mV was evaluated. All voltammogram measurements were obtained under dark conditions to avoid the influence of the light. Several electrolytes were tested for anatase and P25 samples. The first sample submitted to the electrochemical study was anatase; for the electrolytes tested, KOH was selected because the voltammograms showed well-defined peaks. Subsequently, KOH was tested with the P25 pellets, but the results were not satisfactory. Therefore, other electrolytes were tested for the P25 pellets, and the best result was achieved by Na_2HPO_4. Then, electrochemical analyses of anatase were also conducted with the sodium phosphate dibasic for comparison purposes.

UV-Visible diffuse reflectance spectroscopy was used to determine the bandgap and Urbach energies of the sintered pellets with a UV/VIS Spectrometer Lambda 650, Perkin Elmer.

3. Results and Discussion

3.1. Sintering of TiO_2 powders

The anatase green pellets were initially produced with pure deionized water (pH 5.8) and different acetic acid aqueous solutions (25%, 50%, 75%, and 100% v/v) and applied a 624 MPa pressure. The pellets made with just water (Table 1) could not be completely removed from the mold since they were very brittle (Figure S1).

The use of 25% acetic acid solution (An1) resulted in a denser pellet than the ones produced with water (An), but they were also found to be fragile. The use of 50% aqueous acetic acid solution improved the densification. The best green pellets were obtained with 75% and 100% acetic acid solutions, which produced very similar characteristics. Due to the corrosivity of acetic acid, the concentration of 100% was discarded to preserve the mold, and the 75% acetic acid aqueous solution was selected to produce the anatase and P25 pellets.

P25 and anatase specific surface areas obtained by N_2 physisorption characterization were 34 and 8 m^2 g^{-1}, respectively[26]. The P25 sintered pellets were less friable than anatase pellets. According to the physisorption characterization and X-ray diffraction, the major difference was probably the much smaller P25 mean crystallite size (Table 2)[29]. Hence,

Table 2. XRD parameters obtained by Rietveld refinement.

Sample	Anatase				Rutile				Rwp[b]	GOF[c]
	a (nm)	c (nm)	LVOL-IB[a] (nm)	% wt	a (nm)	c (nm)	LVOL-IB (nm)	% wt		
Anatase	3.785	9.516	86 (10)	100.0	-	-	-	-	9.56	1.15
An200	3.785	9.513	116 (17)	100.0	-	-	-	-	6.32	1.21
An400	3.785	9.513	122 (13)	100.0	-	-	-	-	7.76	1.52
An800	3.785	9.515	122 (13)	100.0	-	-	-	-	7.70	1.48
P25	3.786	9.510	18	87.8	4.595	2.960	29	12.2	7.90	1.11
P200	3.855	9.507	18 (15)	88.0	4.594	2.959	29 (13)	12.0	6.72	1.29
P400	3.785	9.508	18(16)	87.9	4.594	2.960	28	12.1	6.74	1.33
P450	3.785	9.508	19 (17)	87.6	4.595	2.959	28 (13)	12.4	6.71	1.29
P500	3.785	9.507	20 (3)	85.8	4.594	2.959	34 (3)	14.2	6.35	1.19

[a]LVOL-IB: crystallite size was determined by the integral breadth[27]. [b]Rwp (weighted pattern): statistical index indicating the minimized residue of Rietveld refinement[28]. [c]GOF (goodness of fit): numerical criterion indicating the quality of Rietveld refinement[28].

the P25 material was expected to provide a better start condition for sintering.

3.2. Fourier transformed infrared spectroscopy

The FTIR analyses of the anatase and P25 raw powders and the pellets AnHAc, An400, An800, PH_2O, PHAc, P250, and P450 are shown in Figures 1 and 2. For the anatase and P25 samples, the bands present at 3400 - 3350 cm^{-1} and 1635 – 1630 cm^{-1} are characteristic of the stretching vibrations ν(O-H) and for the bending vibrations $\delta(H_2O)$ of water molecules, respectively, adsorbed on titania[30-33]. The bands present in the PHAc and P250 samples, at 1540 and 1430 cm^{-1} are attributed to the O-C-O asymmetric and symmetric stretching vibrations (ν(O-C-O)) of acetate[30,34].

The spectra showed the absorption at 1720 cm^{-1} related to C=O stretching vibration (ν(C-O)) of acetic acid due to the free acetic acid molecules with monomeric and dimeric forms[35]. However, the 1540 - 1500 and 1430 - 1420 cm^{-1} doublets indicate the formation of acetates. Then, acetic acid forms a complex with titanium. The frequency separation ($\Delta\nu$) close to 100 cm^{-1} refers to coordination in bidentate geometry[34-36].

The acetate remains on TiO_2 (P25 pellets) up to 400 °C, as shown in Figure 2, which is certainly related to the strong chelating ability. After this temperature (P450), there was no observation of the doublet in the spectrum[34].

Anatase samples FTIR spectra (Figure 1) also showed the acetate species bands, indicating the formation of the bidentate coordination compound.

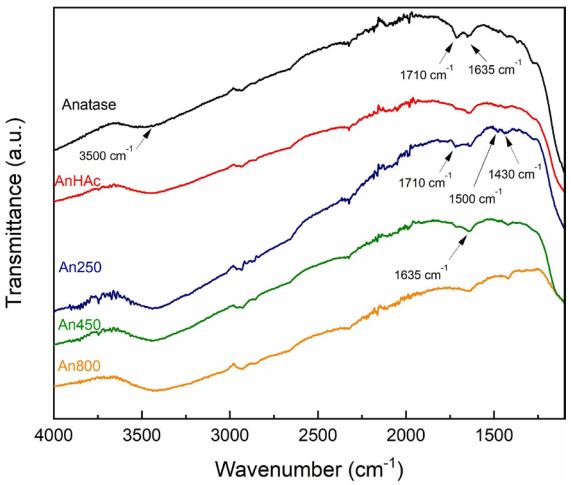

Figure 1. FTIR spectra of samples anatase, AnHAc, An400, An250, and An800.

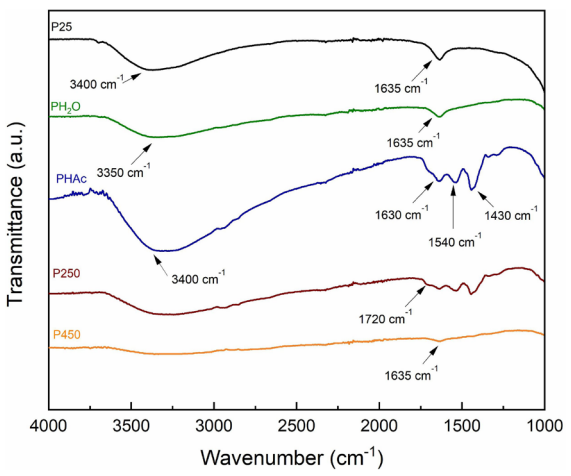

Figure 2. FTIR spectra of samples P25, PHAc, P450, P250, and PH_2O.

3.3. TG/DSC for anatase and P25 pellets

Figure 3a displays the TG / DSC analysis for the anatase sample after mixing and pressing with 0.15 mL 75% of acetic acid solution and 375 MPa. A steep mass loss before 100 °C is observed due to water evaporation. The inset of Figure 3a shows that the first reaction ends at around 119 °C, followed by three, perhaps four, other reactions with loss of mass. The subsequent reactions are probably associated with compounds formed by acetic acid and TiO_2 since the pure acetic acid boiling point is 118 °C[37]. These compounds may play an important role in the low-temperature sintering process since they help to solubilize the TiO_2, but they were not identified.

The DSC curve, the blue line in Figure 3a, indicates the existence of three endothermic peaks. The peak at 88 °C corresponds to the evaporation of water. The peaks at 125 °C and 236 °C are probably related to acetic acid and compounds formed between titania and acetic acid[38,39].

Figure 3b shows the TG / DSC analysis for the P25 pellet after pressing with 0.10 mL of 75% acetic acid solution. The first three endothermic peaks were also observed in the anatase, and there is a fourth broad peak at 313 °C. The fourth peak is probably due to the decomposition of a new compound, not formed with anatase, with a very small loss of mass. Figure S3 displays a comparison of DSC analysis for pure P25, and P25 pellet pressed with the acetic acid solution. No peaks can be observed for pure P25 which confirms that peaks observed for P25 pellet pressed with acetic acid are related to the acetic acid presence.

In Figure 3, the TGA curves showed three weight loss steps for anatase and P25. The first steep step and second step are consistent with water and acetic acid evaporation. The third evaporation step appeared around 250 °C and ended at 400 °C for anatase and continued up to 500°C for the P25 samples[40]. According to the FTIR, the acetate species are present in the P25 samples up to 250 °C but disappear by 400 °C. Therefore, the third step is related to acetate decomposition. The FTIR and TG analyses indicate that acetate species are present in the samples. Therefore, they may help the sintering process during heat treatment.

3.4. Crystallographic characterization

There is no evidence of the rutile phase in the diffractogram of the TiO_2 anatase commercial powder (Figure 4). The XRD patterns of An200, An400 and An800 sintered at 200 °C, 400 °C and 800 °C display only anatase phase. The crystallite size increased for the sintered anatase compared to the powder but did not change with the sintering temperature (Table 2) within the experimental error. The anatase and

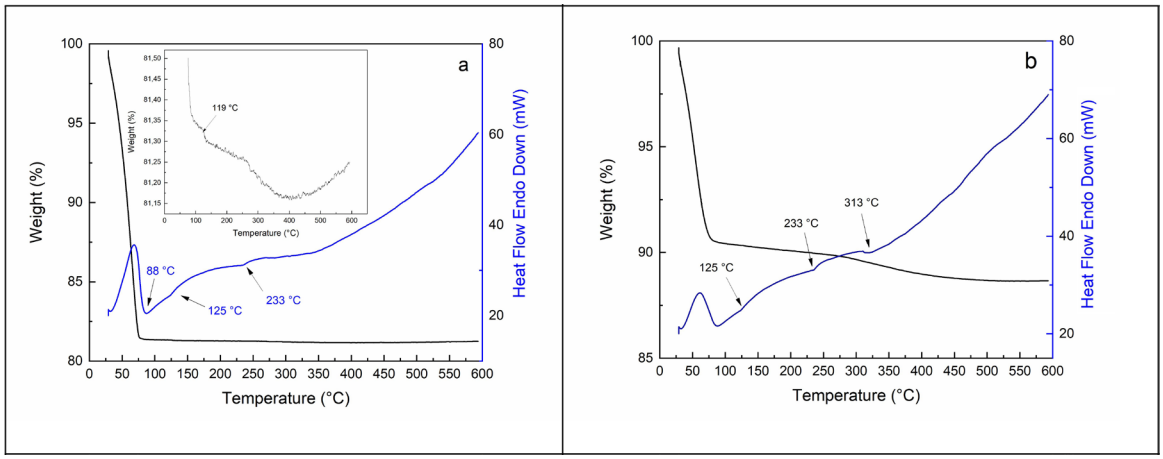

Figure 3. TG and DTG curves of anatase (a), TG curve for anatase, and (b) P25 pellets at the heating rate of 10°C min^{-1}.

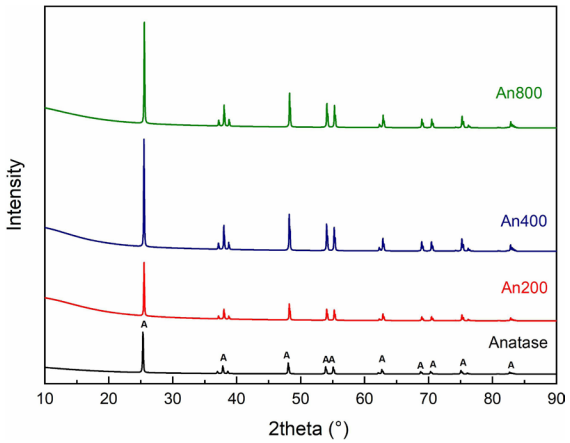

Figure 4. XRD patterns of anatase pellets and anatase commercial starting powder.

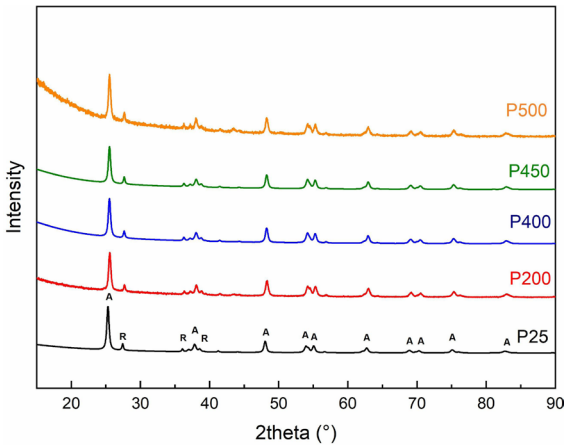

Figure 5. XRD patterns of P25 pellets and P25 commercial starting powder.

rutile crystallite sizes remained the same for powder and sintered pellets of P25.

The diffractogram of the P25 pellets and the P25 powder are shown in Figure 5. The crystallographic information files (CIF) were obtained from the Inorganic Crystal Structure Database (ICSD) by FIZ Karlsruhe[41]. The P25 raw nanopowder consists of a mixture of anatase (87.8% mass) (ICSD 63711) and rutile (12.2% mass) (ICSD 9161) phases (Table 2), determined by the Rietveld method.

The anatase and rutile phases´ mass content does not change up to 500 °C. The rutile mass slightly increased at the highest sintering temperature, as shown in Table 2. Since this result is very close to the experimental errors expected for this characterization, another technique should be employed to confirm this transformation. The anatase to rutile phase transformation was not expected since the sintering temperature was below the phase transformation temperature, 600 °C[16]. This temperature can be even higher when the crystallite size is very small, as observed for the An800 anatase pellet that did not show any phase transformation.

3.5. Densification

The relative densities of the anatase and P25 pellets, produced with 75% acetic acid solution, are listed in Table 3. The densities are the average for all analyzed pellets under a certain condition, and the density measurement for each pellet is also an average value. The anatase pellets' density could only be calculated for pellets sintered at 800 °C. The pellets sintered at lower temperatures (200 °C and 400 °C) disintegrated in water.

The sample with the highest density was anatase pellet sintered at 800 °C, An800, which is consistent with the temperature effect on the sintering process.

Medri et al.[8] produced P25 and anatase pellets by CSP (using 80% of acetic acid solution) and obtained relative densities of 62% and 54% for the P25 using 500 MPa and 250 MPa pressures, respectively. The authors used 80% and 40% of acetic acid solutions for the anatase pellets, with pressures ranging between 250 MPa and 500 MPa. The pellets prepared with 80% of acetic acid solution displayed relative

densities of 53% and 60% after being submitted to 250 and 500 MPa, respectively. The anatase pellet prepared with a 40% acetic acid solution and a pressure of 500 MPa showed a relative density of 57%. The main difference between the work performed by Medri et al. and the present one is the heat treatment of the pellets. In their work, the mold was under constant heating of 150 °C for 30 minutes during the compression. In the present work, the pellets were heat-treated after compression using a conventional oven. The present procedure may have allowed more time for the acid solution to react with TiO_2, which resulted in a slight increase in the P25 relative density compared to Medri et al.[8].

Table 3. Relative density of anatase and P25 pellets after the sintering process, 3.89 and 4.20 g cm $^{-3}$ were their densities measured by X-ray diffraction.

Sample	Density
An800	70.27%
P200	64.10%
P400	66.41%
P450	66.41%
P500	66.03%

The increase in the sintering temperature had a marginal effect on the densification of P25 pellets. Pure acetic acid boils at 118 °C[37]; therefore, no volatile species above this temperature are observed with the TG/DSC (Figure 3) except the acetate decomposition to participate in the sintering process[42].

Medri et al.[8] achieved the highest density of 68% for pellets produced with anatase, using 40% of acetic acid solution, 500 MPa and 150 °C. The present work reached a slightly higher density (Table 3) with a more concentrated acetic acid solution, lower pressure, and conventional heat-treatment after molding the pellet at a relatively high temperature (800 °C).

It can be noticed that Anatase pellets required a much higher sintering temperature than P25. The difference between anatase and P25 samples are the crystalline phases and crystallite mean sizes (Table 2).

3.6. Surface microscopy characterization

3.6.1. Anatase pellets

The SEM images in Figure 6 show the surface of the anatase pellets sintered at 200 ºC, 400 ºC, and 800 ºC

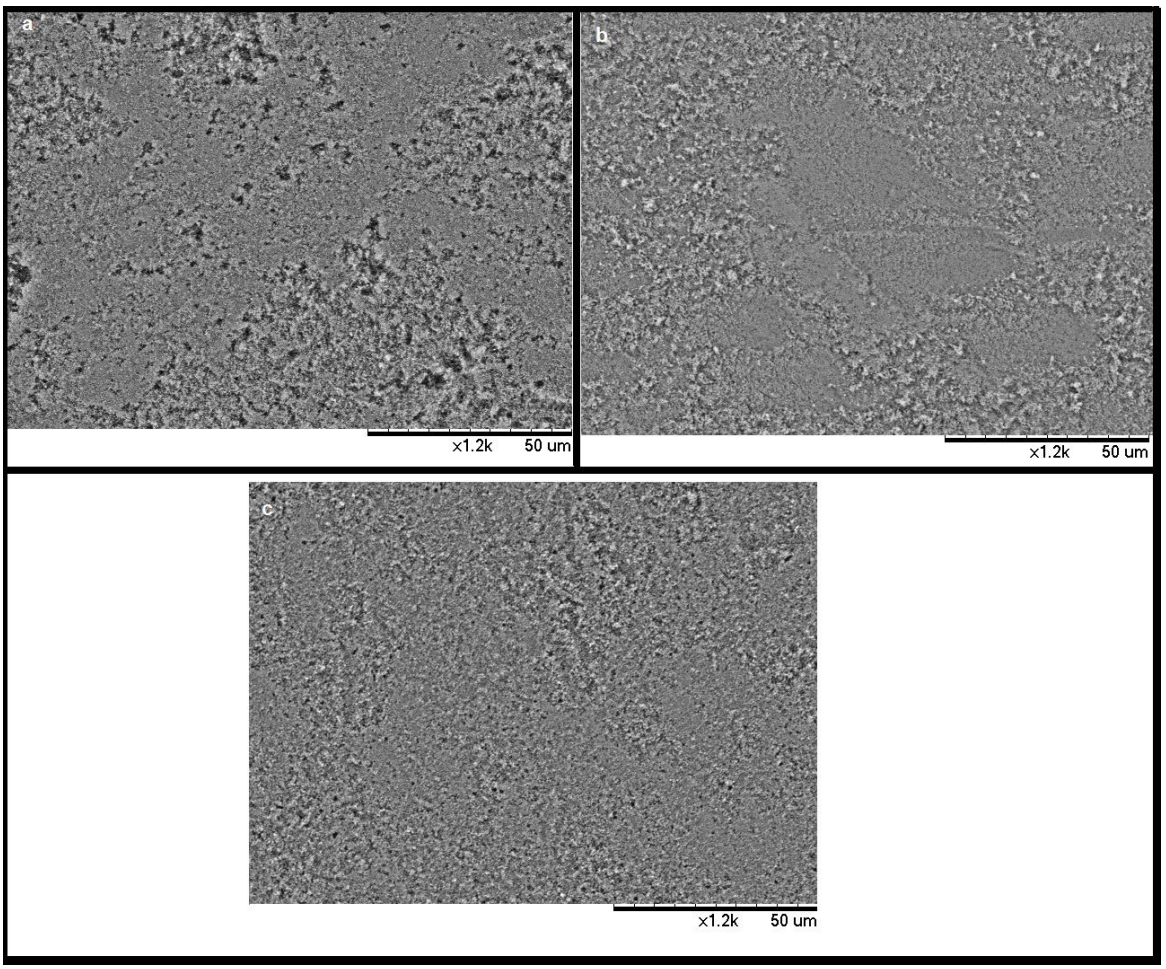

Figure 6. SEM micrographs of the surface of a) An200, b) An400, and c) An800 pellets.

(An200, An400, and An800, respectively). The surface of the An200 pellet (Figure 6a) presented large amounts of holes and particle agglomerates. Thus, its sintering was ineffective, and its integrity was impaired, making the pellet the most fragile among the prepared ones. The An400 surface (Figure 6b) presented smaller holes when compared to those of the An200 pellet. The An400 pellets were less brittle than the An200, but they were still fragile. The An800 pellet presented the best integrity among the anatase samples, and its surface (Figure 6c) presented the least amount of holes. The only difference between these anatase pellets was the temperature, a fundamental parameter, especially in low-temperature sintering processes.

3.6.2. P25 pellets

Figure 7 shows the P25 pellets´ surface. The P200 (Figure 7a) and P500 (Figure 7d) surfaces were rough, with many grooves following grain boundaries, indicating that the sintering conditions were inappropriate. The 200 °C might be too low for sintering. The surface roughness observed for P500 may be associated with the small amount of anatase to rutile phase transformation. This transformation was observed by XRD analysis. It should be noted that the cell volume is 34.061 $Å^3$ for anatase and 31.216 $Å^3$ for rutile[43] which could cause the roughness.

The P400 pellet surface (Figure 7b) was smoother than the P200, so its sintering was more effective than the P200. Another pellet was sintered at 450 °C (P450) (Figure 7c), and its surface was even smoother than the pellet sintered at 400 °C, with almost no visible imperfection. It should be noted that at 450 °C, there was no phase transformation of anatase to rutile (Table 2). The much lower sintering temperature for the P25 pellets compared with the anatase pellets is certainly related to the much smaller crystallite size of the P25 (Table 2).

The acetate compounds observed in the FTIR probably precipitated along the grain boundaries as very small nuclei during the dissociation, then sintering and grain growth probably occurred by the coalescence of these particles. Above 400 °C, TG/DSC analysis showed that the solvent and any formed compound had already disappeared either by evaporation or dissociation and evaporation. This disappearance can be very important depending on the application of these pellets that might require a pure TiO_2. However, the acetic acid solution was beneficial for the sintering process[44].

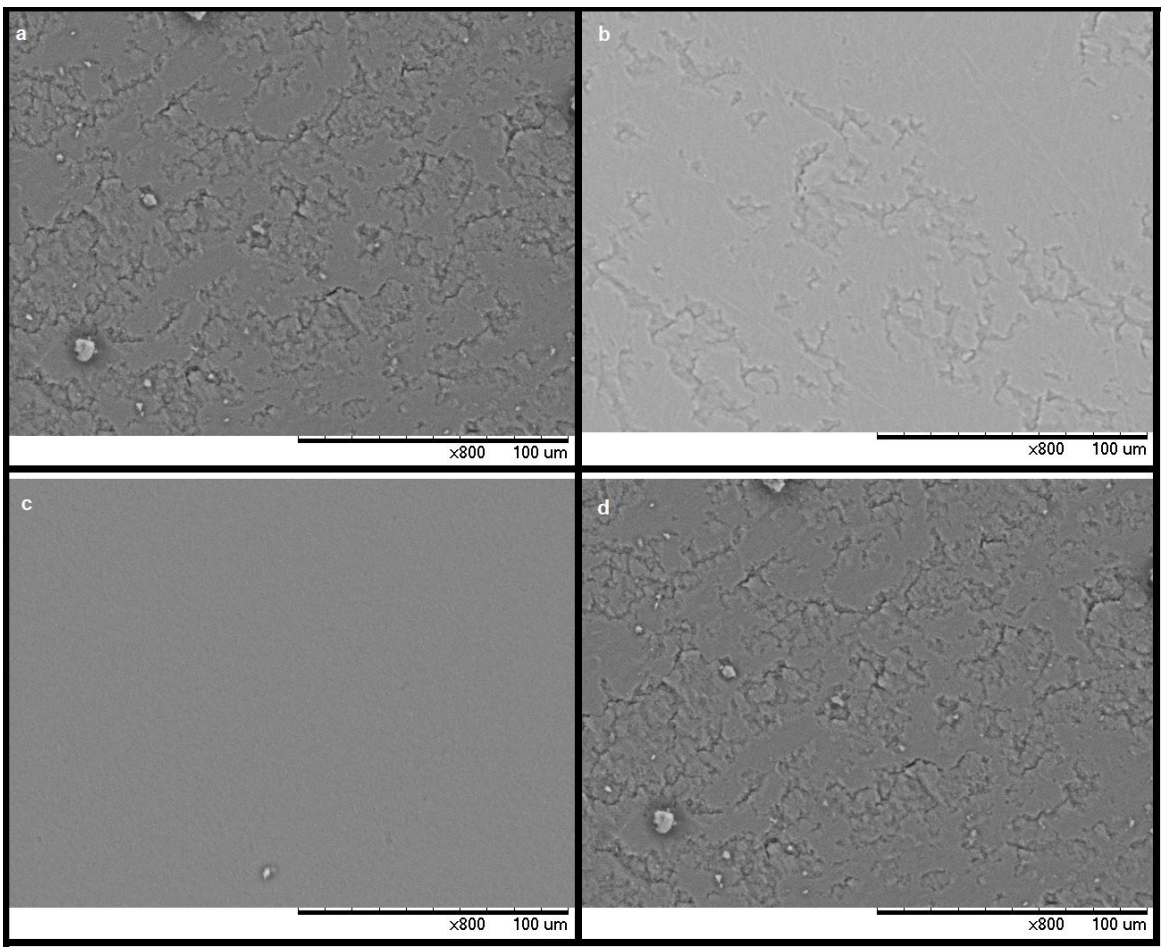

Figure 7. SEM micrographs of the surface of a) P200, b) P400, c) P450, and d) P500 sintered P25 samples.

3.7. Electrochemical study

Figure 8 shows the sample An400 cyclic voltammogram, with a scan rate of 50 mV s^{-1} within the potential range of ±1500 mV and 0.1 mol L^{-1} KOH aqueous solution as the supporting electrolyte (Figure 8)[17]. The observed reduction event, a cathodic peak close to -1180 mV, is characteristic of anatase in the selected electrolytic medium[17] and corresponds to the reduction of Ti^{4+} to Ti^{3+} (Equation 1)[45]. It is related to the titanium atoms acting as electron traps either at oxygen vacancies in the bulk of the TiO_2 or at the interface oxide/electrolyte or conduction band states of the TiO_2. The anodic peak at -380 mV on the scan results from unfilling the trap/conduction band states[25,46]. It was also observed an anodic peak at +1170 mV, which is probably related to the oxidation of the OH^{1-} (Equation 2)[47]

$$TiO_2 + e^{-1} + 4H^+ \rightarrow Ti^{3+} + 2H_2O \quad (1)$$

$$OH^{-1} - e^{-1} \rightarrow \frac{1}{4}O_2 + \frac{1}{2}H_2O \quad (2)$$

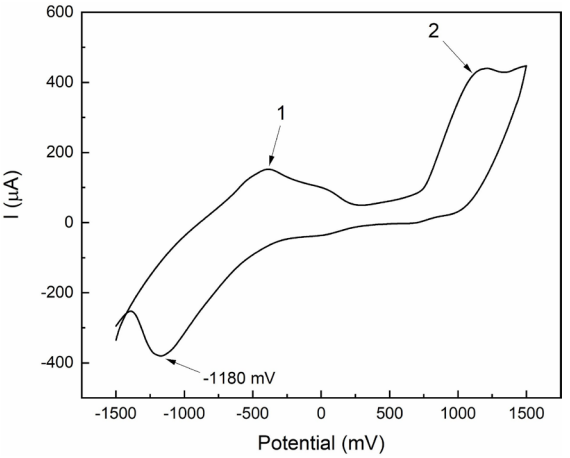

Figure 8. An400 cyclic voltammogram with a scan rate of 50 mV s^{-1} in 0.1 mol L^{-1} KOH solution as supporting electrolyte.

Figure 9a shows the P400 sample, P25 pellet sintered at 400 °C, voltammogram with: two oxidations (anodic peaks - 1 and 2) and two reductions (cathodic peaks - 3 and 4). There was a second anodic peak in addition to the ones observed with An400 (Figure 8). Differences in peak potentials observed using both electrodes might be explained by the different supporting electrolytes (aqueous solution of Na_2HPO_4 in the case of P25) besides the differences imposed by the presence of two phases for the P25 pellets, rutile and anatase, and one phase for the anatase pellets (Table 2). The anodic peak (1) at -200 mV and the cathodic peak[4] at 680 mV form a redox pair (Figure 9b)[48] for the P400 samples, as shown by the dependence between them in the scan made from -1500 mV to +500 mV and their independence from the peaks (2) and (3) observed in Figure 9b. The presence of peaks 1 and 4 (Figure 9b) indicates that the material is porous, a consequence of the sintering process. Capacitance is considered a characteristic of porous electrodes. Its behavior is influenced by the transfer rate between charges, that are dependent on the redox species present, as well as the superposition of electronic levels on the surface of the material, observed in Figure 9b with the presence of a redox pair[49].

Porous semiconductor electrodes behave as capacitors, accumulating charge when a critical applied voltage is achieved, for example, in a cyclic voltammetry experiment[49]. Fabregat-Santiago et al. stated that if nanoparticles, such as the P25, do not contain dopants, one can control the Fermi level of the electron if the particle sizes are very small and have enough electrical conductivity. The conduction band displacement controls the Fermi level, and hence there is an increase in the concentration of electrons in that region. This change in the material corresponds to an intrinsic capacitance.

The comparison of voltammograms for the four P25 sintering temperatures (Figure 10) shows the shift of the observed peaks. This difference might be related to the samples' porosity[49,50] as the degree of sintering varied for each applied temperature. However, it was impossible to observe a consistent change of the peak charge transferred to the electrode before the first peak current maximum is reached as a temperature function, as proposed by Zhu and

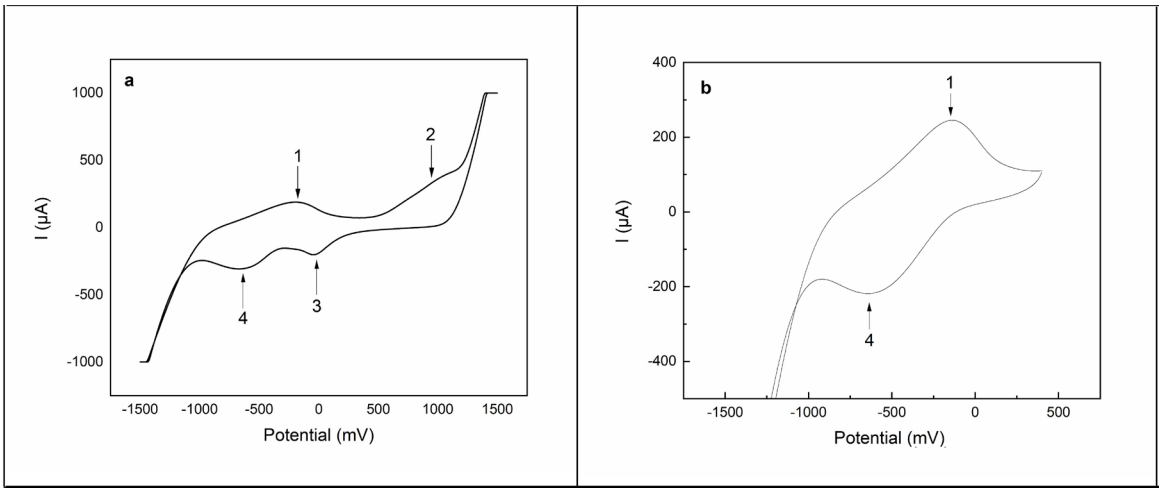

Figure 9. a) P400 voltammogram and b) possible redox pairs, with a scan rate of 100 mV s^{-1}, and 0.5 mol L^{-1} Na_2HPO_4.

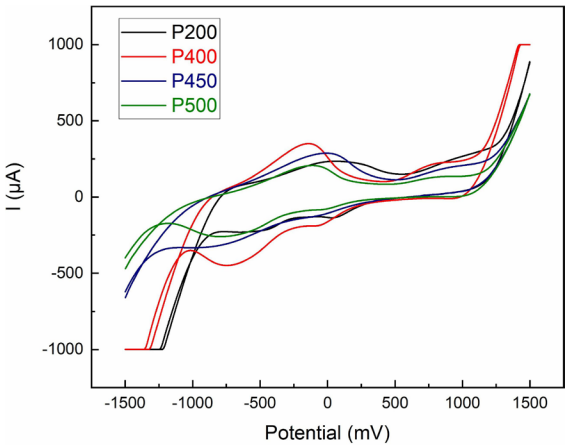

Figure 10. Cyclic voltammograms of P25 with different sintering temperatures. Scan rate of 50 mV s^{-1} in 0.5 mol L^{-1} Na_2HPO_4.

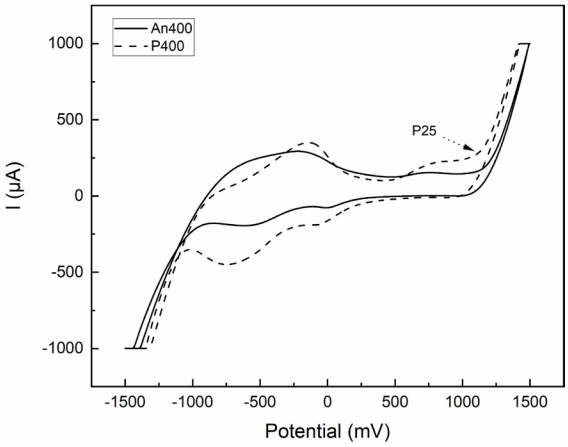

Figure 11. Cyclic voltammograms of P400 (dashed line) and An400 (solid line). Scan rate of 50 mV s^{-1} in 0.5 mol L^{-1} Na_2HPO_4.

Zhao[50]. So it is suggested that another mechanism is also present, with the capacitance increasing due to the surface area. This mechanism might be related to the color change of the P25 pellets observed after the voltammetry (Figure 10).

Comparing the An400 and P400 cyclic voltammograms (Figure 11), it can be noticed that despite the similarity in the voltammogram profiles, the oxidation and reduction peaks of P400 are better defined, and their potentials are slightly shifted. Such a difference might be due to the crystallite sizes. The much smaller P400 particle size will result in larger capacitance, therefore, stronger peaks.

During the CV analysis, the P25 pellets developed blue spots that ended up covering their surfaces, as seen in Figure 12. However, the original color was recovered after exposing the pellets to air[51]. The anatase pellets did not change their color when submitted to CV analysis. Hence the blue color results from oxygen vacancies on the surface, or just below, of the rutile phase present in P25[52]. The oxygen vacancies reduce Ti^{4+} to Ti^{3+}, mainly in the rutile phase, giving the blue color[51].

Huo et al. observed similar behavior with color-changing during the hydrogenation process of TiO_2 nanoparticles, which removes oxygen from the titanium oxide crystal structure[52], thus relating that to the Ti (IV) reduction. The present study accomplished such an effect by applying a potential difference.

3.8. Diffuse reflectance spectroscopy UV-Vis (DRS).

The P400, P450, and P500 pellets were analyzed before cyclic voltammetry and after (when the surface became blue). Table 4 displays the calculated bandgaps and Urbach energies for all samples. The bandgaps are close to the rutile bandgap due to the P25´s very small crystallite. It was expected that the blue material had a lower bandgap value, but only the surface of the pellet had this color and the material had to be grounded before the analysis. Thus, the analysis was

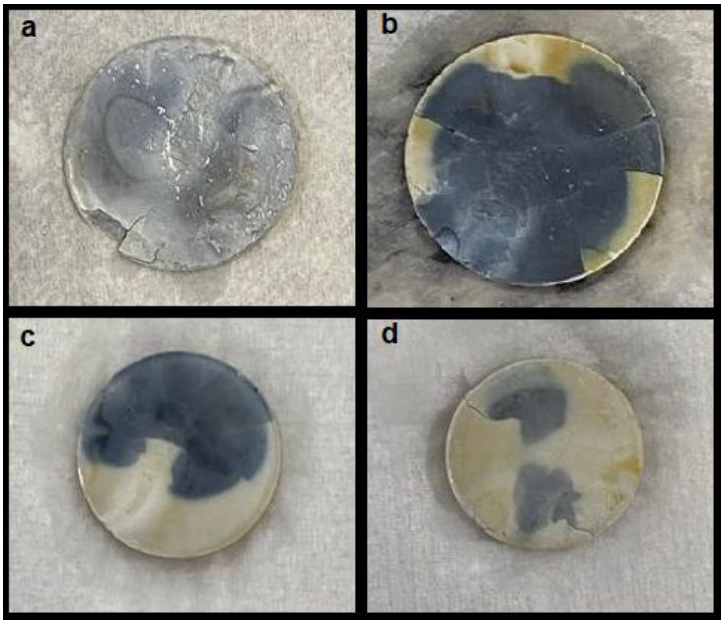

Figure 12. a) P200, b) P400, c) P450 and d) P500 after CV analysis.

Table 4. Bandgap values and Urbach energy for anatase, rutile, P400, P400 blue, P450, P450 blue, and P500 samples.

Samples	Bang gap energy (eV)	Standard error	Urbach Energy (eV)
Anatase	3.20 [43]	-	-
Rutile	3.00 [43]	-	-
P25	3.25 [44]	-	-
P400	3.01	0.02	0.072
P400 blue	2.97	0.22	0.079
P450	2.98	0.03	0.096
P450 blue	2.96	0.10	0.102
P500	2.99	0.02	0.074

performed with a mixture of the blue material (from the surface) and the original material (inside the pellet).

After voltammetry, the pellets with blue color showed a greater Urbach energy than the samples before applying the potential cycle. Increased Urbach energy is related to defects in the semiconductor crystalline structure, with energies inside the bandgap near the conduction or valence band. Defects such as oxygen vacancy and the reduction of titanium in Ti^{3+} result in this bluish color[53,54]. It is worth mentioning that the blue color was reversible, when the pellets were exposed to atmospheric air, they regained their original color.

4. Conclusion

A low-temperature sintering process successfully produced anatase and P25 pellets using acetic acid as a transient liquid during the green body pressing followed by a sintering in a typical furnace at a low temperature. For anatase, the best sintering temperature was 800 ºC, while 450 ºC provided the best result for P25 material, which remained with the same anatase to rutile phase ratio. Besides the use of less energy, the absence of phase transformation of anatase to rutile is the main reason for using a low-sintering temperature instead of the conventional sintering process. Mixing the raw powders with an acetic acid aqueous solution (at 75% v/v) was a requirement to achieve low-temperature sintering. The acetic acid reacted with the titanium oxide at room temperature and produced titanium acetates that were present up to 400 ºC. The proposed method differs from the cold sintering process because the heating is performed after the wet powder compression. The approach studied is very promising since good results were obtained without requiring special equipment to heat the sample under pressure inside the mold. Cyclic voltammetry indicated that the sintered TiO_2 pellets are porous with a partial capacitive response, an important characteristic for catalytic and photocatalytic applications. The applied tension produced vacancies inside the TiO_2 bandgap that changed the pellet´s surface color and this was confirmed by the increased Urbach energy. The bandgaps for anatase and P25 pellets had the same values within the standard error. It was verified, then, that the low-temperature sintering method proposed did not change the bandgap nor the crystalline phases. Therefore, it is a promising method that could be applied for several photocatalysts based on titania, improving the photocatalyst recovery after the reaction.

5. Acknowledgments

Ricardo Aucelio, Roberto de Avillez, and Sonia Letichevsky thank grants from Brazilian agencies FAPERJ (E-26/202.912/2017, E-26/202.870/2018, and E-26/010.000982/2019), and CNPq (303866/2017-9 and 304015/2019-9). Anna Luísa Miguel thanks Coordenação de Aperfeiçoamento de Pessoal de Nível Superior – Brasil (CAPES) - Finance Code 001. The authors thank Evonik for providing the P25 samples. The authors thank the Bojan Marinkovic and Marco Cremona research groups for the thermogravimetric and DRS, and FTIR analyses, respectively.

6. References

1. Morales J, Maldonado A, Olvera ML. Synthesis and characterization and photocatalytic activity of TiO_2 powders. In: 2016 13th International Conference on Electrical Engineering, Computing Science and Automatic Control (CCE); 2016; Mexico City, Mexico. Proceedings. New York: IEEE; 2016.
2. Pestana CJ, Robertson PKJ, Edwards C, Wilhelm W, McKenzie C, Lawton LA. A continuous flow packed bed photocatalytic reactor for the destruction of 2-methylisoborneol and geosmin utilising pelletised TiO_2. Chem Eng J. 2014;235:293-8.
3. Luo Z, Li Z, Xie Z, Sokolova IM, Song L, Peijnenburg WJGM, et al. Rethinking nano-TiO_2 safety: overview of toxic effects in humans and aquatic animals. Small. 2020;16(36):1-18.
4. Skocaj M, Filipic M, Petkovic J, Novak S. Titanium dioxide in our everyday life; Is it safe? Radiol Oncol. 2011;45(4):227-47.
5. Yildiz T, Yatmaz HC, Öztürk K. Anatase TiO_2 powder immobilized on reticulated Al_2O_3 ceramics as a photocatalyst for degradation of RO16 azo dye. Ceram Int. 2020;46(7):8651-7.
6. Daniel D, Gutz IGR. Microfluidic cell with a TiO_2 -modified gold electrode irradiated by an UV-LED for in situ photocatalytic decomposition of organic matter and its potentiality for voltammetric analysis of metal ions. Electrochem Commun. 2007;9:522-8.
7. Funahashi S, Guo J, Guo H, Wang K, Baker AL, Shiratsuyu K, et al. Demonstration of the cold sintering process study for the densification and grain growth of ZnO ceramics. J Am Ceram Soc. 2017;100(2):546-53.
8. Medri V, Servadei F, Bendoni R, Natali Murri A, Vaccari A, Landi E. Nano-to-macroporous TiO_2 (anatase) by cold sintering process. J Eur Ceram Soc. 2019;39(7):2453-62.
9. Guo H, Guo J, Baker A, Randall CA. Hydrothermal-assisted cold sintering process: a new guidance for low-temperature ceramic sintering. ACS Appl Mater Interfaces. 2016;8(32):20909-15.
10. Ndayishimiye A, Sengul MY, Bang SH, Tsuji K, Takashima K, Hérisson de Beauvoir T, et al. Comparing hydrothermal sintering and cold sintering process: mechanisms, microstructure, kinetics and chemistry. J Eur Ceram Soc. 2020;40(4):1312-24.
11. Guo J, Baker AL, Guo H, Lanagan M, Randall CA. Cold sintering process: a new era for ceramic packaging and microwave device development. J Am Ceram Soc. 2017;100(2):669-77.
12. Maria J-P, Kang X, Floyd RD, Dickey EC, Guo H, Guo J, et al. Cold sintering : current status and prospects. J Mater Res. 2017;32(17):3205-18.
13. Guo J, Floyd R, Lowum S, Maria J-P, Herisson de Beauvoir T, Seo J-H, et al. Cold sintering: progress, challenges, and future opportunities. Annu Rev Mater Res. 2019;49(1):275-95.
14. Grasso S, Biesuz M, Zoli L, Taveri G, Duff AI, Ke D, et al. A review of cold sintering processes. Adv Appl Ceramics. 2020;119(3):115-43.
15. Guo J, Guo H, Baker AL, Lanagan MT, Kupp ER, Messing GL, et al. Cold sintering: a paradigm shift for processing and integration of ceramics. Angew Chem Int Ed. 2016;55(38):11457-61.

16. Hanaor DAH, Sorrell CC. Review of the anatase to rutile phase transformation. J Mater Sci. 2011;46(4):855-74.
17. Cabello G, Davoglio RA, Pereira EC. Microwave-assisted synthesis of anatase-TiO_2 nanoparticles with catalytic activity in oxygen reduction. J Electroanal Chem. 2017;794(April):36-42.
18. Elgrishi N, Rountree KJ, McCarthy BD, Rountree ES, Eisenhart TT, Dempsey JL. A practical beginner's guide to cyclic voltammetry. J Chem Educ. 2018;95(2):197-206.
19. Falk GS, Yesid Gómez González S, Hotza D. Low-energy microwave synthesis and cold sintering of nanograined TiO_2-Nb_2O_5. Mater Lett. 2020;278:128418.
20. Doebelin N, Kleeberg R. Profex: a graphical user interface for the Rietveld refinement program BGMN. J Appl Cryst. 2015;48(5):1573-80.
21. Mittemeijer EJ, Welzel U. The "state of the art" of the diffraction analysis of crystallite size and lattice strain. Zeitschrift fur Krist. 2008;223(9):552-60.
22. Ortiz AL, Cumbrera FL, Sánchez-Bajo F, Guiberteau F, Caruso R. Fundamental parameters approach in the Rietveld method: a study of the stability of results versus the accuracy of the instrumental profile. J Eur Ceram Soc. 2000;20(11):1845-51.
23. Muniz FTL, Miranda MAR, Morilla dos Santos C, Sasaki JM. The Scherrer equation and the dynamical theory of X-ray diffraction. Acta Crystallogr A Found Adv. 2016;72(3):385-90.
24. Rabier F, Temmerman M, Böhm T, Hartmann H, Daugbjerg Jensen P, Rathbauer J, et al. Particle density determination of pellets and briquettes. Biomass Bioenergy. 2006;30(11):954-63.
25. Topoglidis E, Campbell CJ, Cass AEG, Durrant JR. Factors that affect protein adsorption on nanostructured titania films. a novel spectroelectrochemical application to sensing. Langmuir. 2001;17(25):7899-906.
26. Martins PRN de A. Óxidos semicondutores nanoestruturados para a fotólise da água: titanatos de zinco e cobalto [dissertação]. Rio de Janeiro: Pontifícia Universidade Católica do Rio de Janeiro; 2018.
27. Cullity BD. Elements of X-ray diffraction. 2nd ed. Phillippines: Addinson-Wesley Publishing Company; 1978. 269 p.
28. Toby BH. R factors in Rietveld analysis: how good is good enough? Powder Diffr. 2006;21(1):67-70.
29. Rahimian M, Ehsani N, Parvin N, Baharvandi H. The effect of particle size, sintering temperature and sintering time on the properties of Al-Al_2O_3 composites, made by powder metallurgy. J Mater Process Technol. 2009;209(14):5387-93
30. Zhang H, Zhou P, Ji H, Ma W, Chen C, Zhao J. Enhancement of photocatalytic decarboxylation on TiO_2 by water-induced change in adsorption-mode. Appl Catal B. 2017;2018(224):376-82.
31. Yu F, Bai X, Yang C, Xu L, Ma J. Reduced graphene oxide–P25 nanocomposites as efficient photocatalysts for degradation of bisphenol A in water. Catalysts. 2019;9(7):607.
32. Martins NCT, Ângelo J, Girão AV, Trindade T, Andrade L, Mendes A. N-doped carbon quantum dots/TiO_2 composite with improved photocatalytic activity. Appl Catal B. 2016;193:67-74.
33. Antić Ž, Krsmanović RM, Nikolić MG, Marinović-Cincović M, Mitrić M, Polizzi S, et al. Multisite luminescence of rare earth doped TiO_2 anatase nanoparticles. Mater Chem Phys. 2012;135(2–3):1064-9.
34. Kignelman G, Thielemans W. Synergistic effects of acetic acid and nitric acid in water-based sol–gel synthesis of crystalline TiO_2 nanoparticles at 25 °C. J Mater Sci. 2021;56(30):16877-86.
35. Elghniji K, Anna-Rabah Z, Elaloui E. Novel and facile synthesis of transparent-monolithic TiO_2 gels by sol-gel method based on an esterification reaction. Mater Sci Pol. 2016;34(3):633-40.
36. Doeuff S, Henry M, Sanchez C, Livage J. Hydrolysis of titanium alkoxides: modification of the molecular precursor by acetic acid. J Non-Cryst Solids. 1987;89(1–2):206-16.
37. Okoye PU, Abdullah AZ, Hameed BH. Synthesis of oxygenated fuel additives via glycerol esterification with acetic acid over bio-derived carbon catalyst. Fuel. 2017;209:538-44.
38. Deshmane VG, Owen SL, Abrokwah RY, Kuila D. Mesoporous nanocrystalline TiO_2 supported metal (Cu, Co, Ni, Pd, Zn, and Sn) catalysts: effect of metal-support interactions on steam reforming of methanol. J Mol Catal Chem. 2015;408:202-13.
39. Egashira M, Kawasumi S, Kagawa S, Seiyama T. Temperature programmed desorption study of water adsorbed on metal oxides. I. Anatase and rutile. Bull Chem Soc Jpn. 1978;51(11):3144-9.
40. Yang K, Peng H, Wen Y, Li N. Re-examination of characteristic FTIR spectrum of secondary layer in bilayer oleic acid-coated Fe_3O_4 nanoparticles. Appl Surf Sci. 2010;256(10):3093-7.
41. Zagorac D, Muller H, Ruehl S, Zagorac J, Rehme S. Recent developments in the Inorganic Crystal Structure Database: theoretical crystal structure data and related features. J Appl Cryst. 2019;52(5):918-25.
42. Askeland DR, Fuulay PP, Wright WJ. Materials science and engineering. 6th ed. Boston: Cengage Learning; 2010. 917 p.
43. Gupta SM, Tripathi M. A review of TiO_2 nanoparticles. Chin Sci Bull. 2011;56(16):1639-57.
44. Guo H, Baker A, Guo J, Randall CA. Cold sintering process: a novel technique for low-temperature ceramic processing of ferroelectrics. J Am Ceram Soc. 2016;3507(38863):3489-507.
45. Chaudhari P, Chaudhari V, Mishra S. Low temperature synthesis of mixed phase titania nanoparticles with high yield, its mechanism and enhanced photoactivity. Mater Res. 2016;19(2):446-50.
46. Rothenberger G, Fitzmaurice D, Graetzel M. Spectroscopy of conduction band electrons in transparent metal oxide semiconductor films: optical determination of the flatband potential of colloidal titanium dioxide films. J Phys Chem. 1992;96(14):5983-6.
47. Ghanem MA, El-Hallag IS, Amer MS, Alotaibi NH. Characteristics of the voltammetric behavior of the hydroxide ion oxidation at disordered mesoporous titanium dioxide electrocatalyst. J Saudi Chem Soc. 2021;25(7):101274.
48. Vajedi FS, Dehghani H. Synthesis of titanium dioxide nanostructures by solvothermal method and their application in preparation of nanocomposite based on graphene. J Mater Sci. 2016;51(4):1845-54.
49. Fabregat-Santiago F, Mora-Seró I, Garcia-Belmonte G, Bisquert J. Cyclic voltammetry studies of nanoporous semiconductors: capacitive and reactive properties of nanocrystalline TiO_2 electrodes in aqueous electrolyte. J Phys Chem B. 2003;107(3):758-68.
50. Zhu P, Zhao Y. Cyclic voltammetry measurements of electroactive surface area of porous nickel: peak current and peak charge methods and diffusion layer effect. Mater Chem Phys. 2019;233:60-7.
51. He KF, Xu EN, Liu Y, Chen WP. Hydrogenation of nano-structured TiO_2 photocatalyst through an electrochemical method. J Nanosci Nanotechnol. 2015;15(1):303-8.
52. Qiu J, Li S, Gray E, Liu H, Gu Q, Sun C, et al. Hydrogenation synthesis of blue TiO_2 for high-performance lithium- ion batteries. J Phys Chem C. 2014;118(17):8824-30.
53. Yu X, Kim B, Kim YK. Highly enhanced photoactivity of anatase TiO_2 nanocrystals by controlled hydrogenation-induced surface defects. ACS Catal. 2013;3(11):2479-86.
54. Ayik C, Studenyak I, Kranjec M, Kurik M. Urbach rule in solid state physics. Int J Opt Appl. 2014;4(3):76-83.

Supplementary material

The following online material is available for this article:

Figure S1 - Pellets of (a) Anatase and (b) P25.

Figure S2 - Mold used to prepare the anatase and P25 pellets.

Figure S3 - Comparison of DSC analysis for pure P25 and P25 pellet pressed with the acetic acid solution.